BNL-212401-2019-JAAM

Optical and photoemission investigation of structural and magnetic transitions in the iron-based superconductor Sr0:67Na0:33Fe2As2

R. Yang, C. C. Homes

To be published in "Physical Review B"

December 2019

Condensed Matter Physics and Materials Science Department

Brookhaven National Laboratory

U.S. Department of Energy

USDOE Office of Science (SC), Basic Energy Sciences (BES) (SC-22)

DISCLAIMER

PHYSICAL REVIEW B **00**, 005100 (2019)

Optical and photoemission investigation of structural and magnetic transitions in the iron-based superconductor $Sr_{0.67}Na_{0.33}Fe_2As_2$

R. Yang,[1,2,3,*] J. W. Huang,[2,3] N. Zaki,[1] I. Pletikosić,[1,4] Y. M. Dai,[5] H. Xiao,[6] T. Valla,[1] P. D. Johnson,[1] X. J. Zhou,[2,3,7,8]
X. G. Qiu,[2,3,7,†] and C. C. Homes[1,‡]
[1]*Condensed Matter Physics and Materials Science Division, Brookhaven National Laboratory, Upton, New York 11973, USA*
[2]*Beijing National Laboratory for Condensed Matter Physics, Institute of Physics, Chinese Academy of Sciences, Beijing 100190, China*
[3]*School of Physical Sciences, University of Chinese Academy of Sciences, Beijing 100049, China*
[4]*Department of Physics, Princeton University, Princeton, New Jersey 08544, USA*
[5]*Center for Superconducting Physics and Materials, National Laboratory of Solid State Microstructures and Department of Physics, Nanjing University, Nanjing 210093, China*
[6]*Center for High Pressure Science and Technology Advanced Research, Beijing 100094, China*
[7]*Songshan Lake Materials Laboratory, Dongguan 523808, China*
[8]*Beijing Academy of Quantum Information Science, Beijing 100193, China*

(Received 1 October 2019; published xxxxxx)

We report the temperature-dependent optical conductivity and angle-resolved photoemission spectroscopy (ARPES) studies of the multiband iron-based superconductor $Sr_{0.67}Na_{0.33}Fe_2As_2$. Measurements were made in the high-temperature tetragonal paramagnetic phase, below the structural and magnetic transitions at $T_N \simeq 125$ K in the orthorhombic spin-density-wave (SDW)-like phase and $T_r \simeq 42$ K in the reentrant tetragonal double-$\mathbf{Q}$ magnetic phase where both charge and SDW order exist, and below the superconducting transition at $T_c \simeq 10$ K. The free-carrier component in the optical conductivity is described by two Drude contributions: one strong and broad and the other weak and narrow. The broad Drude component decreases dramatically below T_N and T_r, with much of its strength being transferred to a bound excitation in the midinfrared, while the narrow Drude component shows no anomalies at either of the transitions, actually increasing in strength at low temperature while narrowing dramatically. The behavior of an infrared-active mode suggests zone folding below T_r. Below T_c the dramatic decrease in the low-frequency optical conductivity signals the formation of a superconducting energy gap. ARPES reveals holelike bands at the center of the Brillouin zone (BZ), with both electron- and holelike bands at the corners. Below T_N, the hole pockets at the center of the BZ decrease in size, consistent with the behavior of the broad Drude component; however, below T_r the electronlike bands shift and split, giving rise to a low-energy excitation in the optical conductivity at $\simeq$20 meV. The C_2 and C_4 magnetic states, with resulting spin-density-wave and charge-SDW order, respectively, lead to a significant reconstruction of the Fermi surface that has profound implications for the transport originating from the electron and hole pockets but appears to have relatively little impact on the superconductivity in this material.

DOI: 10.1103/PhysRevB.00.005100

I. INTRODUCTION

The discovery of iron-based superconductors prompted an intensive investigation in the hope of identifying new compounds with high superconducting critical temperatures T_c [1–4]. In many of the iron-based materials, superconductivity emerges with the suppression of antiferromagnetic (AFM) order, suggesting that the pairing mechanism is related to the magnetism. Indeed, the iron-based materials display a variety of magnetically ordered ground states [5–9] that may either compete with or foster the emergence of superconductivity.

One class of materials, $A\mathrm{Fe_2As_2}$, where $A =$ Ba, Ca, or Sr (the so-called 122 materials), is particularly useful as superconductivity may be induced through a variety of chemical substitutions [10–20], as well as through the application of pressure [21–24]. The phase diagram of $Sr_{1-x}Na_xFe_2As_2$ has a number of interesting features. At room temperature, the parent compound $SrFe_2As_2$ is a paramagnetic metal with a tetragonal ($I4/mmm$) structure. The resistivity in the iron-arsenic planes decreases with temperature until it drops anomalously as the material undergoes a magnetic transition at $T_N \simeq 195$ K to a spin-density-wave (SDW)-like AFM ground state that is also accompanied by a structural transition to an orthorhombic ($Fmmm$) phase [25–30]. The crystals are heavily twinned in the orthorhombic phase; however, the application of uniaxial stress along the (110) direction of the tetragonal unit cell results in a nearly twin-free sample [31,32]. The magnetic order may be described as AFM stripes, where the iron spins are aligned antiferromagnetically along

---

[*] Present address: Laboratorium für Festkörperphysik, ETH Zürich, CH-8093 Züich, Switzerland.

[†] xgqiu@iphy.ac.cn

[‡] homes@bnl.gov

the *a* axis and ferromagnetically along the *b* axis [33,34]; this is also referred to as the magnetic C_2 phase due to its twofold rotation symmetry. As the sodium content increases, the magnetic and structural transition temperatures decrease until both disappear at $x \simeq 0.48$; superconductivity appears well before this point at $x \simeq 0.2$ and reaches a maximum of $T_c \simeq 37$ K for $x \simeq 0.5$–0.6. Between $0.29 < x < 0.42$, an additional magnetic and structural transition occurs below $T_{\rm N}$ at T_r; the tetragonal ($I4/mmm$) phase reemerges, forming a dome which lies completely within the AFM region. This phase appears to be a common element in the hole-doped 122 materials [35–45]; however, in $\mathrm{Sr}_{1-x}\mathrm{Na}_x\mathrm{Fe}_2\mathrm{As}_2$ the dome is more robust and occurs over a wider doping range at temperatures up to $T_r \simeq 65$ K [39,40], which is higher than what has been observed in other compounds. This magnetic order is described as the collinear superposition of two itinerant SDWs with nesting wave vector $\mathbf{Q}$, leading to a double-$\mathbf{Q}$ SDW [44,45] in which half the iron sites are nonmagnetic and half have twice the moment measured in the orthorhombic AFM phase, oriented along the *c* axis [46,47]; this is referred to as the magnetic C_4 phase because of its fourfold rotational invariance. This magnetic state is accompanied by a charge-density wave (CDW) with the charge coupling to the square of the magnetization, resulting in a charge-SDW (CSDW) [48].

In this work, the complex optical properties and angle-resolved photoemission spectroscopy (ARPES) of $\mathrm{Sr}_{0.67}\mathrm{Na}_{0.33}\mathrm{Fe}_2\mathrm{As}_2$ are investigated in the high-temperature tetragonal phase, as well as the magnetic C_2 and C_4 phases. The value of $x \simeq 0.33$ used in the current study is slightly below the optimal value of $x \simeq 0.37$ that bisects the C_4 dome in the $\mathrm{Sr}_{1-x}\mathrm{Na}_x\mathrm{Fe}_2\mathrm{As}_2$ phase diagram [39]. Based on transport studies, $T_{\rm N} \simeq 125$ K, $T_r \simeq 42$ K, and $T_c \simeq 10$K. In the high-temperature tetragonal paramagnetic state, the optical response of the free carriers is described by two Drude terms (Sec. IIIA): one strong and broad (large scattering rate) and the other weak and narrower (smaller scattering rate); as the temperature is reduced, the strength of the Drude terms shows relatively little temperature dependence, while the scattering rates slowly decrease. Below $T_{\rm N}$, the Fermi surface reconstruction driven by the structural and magnetic transitions causes both the strength and the scattering rate for the broad Drude term to decrease dramatically; the missing spectral weight (the area under the conductivity curve) associated with the free carriers is transferred to a peak that emerges in the midinfrared. The narrow Drude term actually increases slightly in strength below $T_{\rm N}$ while narrowing. Below T_r, in the magnetic C_4 phase, the broad Drude term again narrows and decreases in strength; while the strength of the narrow term does not appear to change, its scattering rate decreases dramatically. Based on the behavior of an infrared-active lattice mode, the presence of CSDW order likely results in the formation of a supercell resulting in zone folding, leading to a further reconstruction of the Fermi surface; while spectral weight is again transferred from the broad Drude to the midinfrared peak, a new low-energy peak emerges at ≃20 meV. Below T_c, there is a dramatic decrease in the low-frequency conductivity, signaling the formation of a superconducting energy gap. ARPES reveals several large hole pockets at the center of the Brillouin zone above $T_{\rm N}$, one of which shifts below the Fermi level below $T_{\rm N}$ in the C_2 magnetic phase, a trend which continues below T_r, suggesting that these bands may be related to the broad Drude response. At the corners of the Brillouin zone, there are both hole- and electronlike bands. Below $T_{\rm N}$ and T_r, several of these bands appear to split and shift, but it is not clear if there are any significant changes to the size of the associated Fermi surfaces, suggesting that some of these carriers may be related to the narrow Drude term; below T_r the band splitting is likely responsible for the emergence of the low-energy peak. The structural and magnetic transitions from which the C_2 (SDW) and C_4 (double-$\mathbf{Q}$ SDW) phases emerge result in a Fermi surface reconstruction that has profound effects on the optical conductivity and electronic structure; however, the superfluid stiffness appears to be more or less unaffected by the CSDW order.

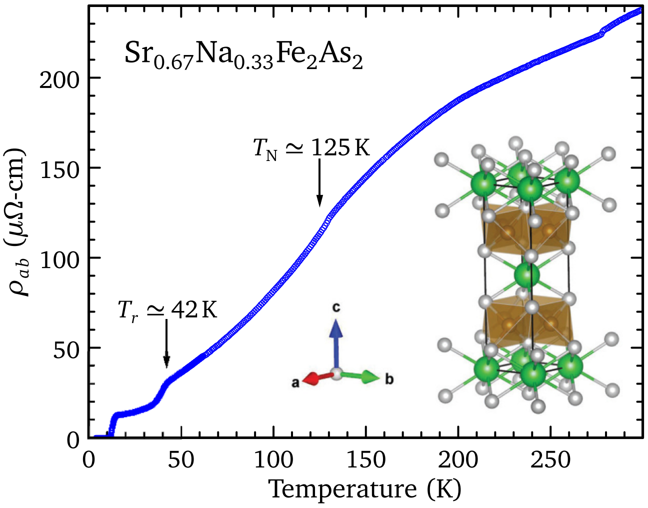

FIG. 1. The temperature dependence of the in-plane resistivity for $\mathrm{Sr}_{0.67}\mathrm{Na}_{0.33}\mathrm{Fe}_2\mathrm{As}_2$ with inflection points at $T_{\rm N} \simeq 125$ K and $T_r \simeq 42$ K; the resistivity at room temperature has been adjusted to match the optical conductivity in the zero-frequency limit. Inset: The generic unit cell in the high-temperature tetragonal phase for the 122 materials.

II. EXPERIMENT

High-quality single crystals of $\mathrm{Sr}_{0.67}\mathrm{Na}_{0.33}\mathrm{Fe}_2\mathrm{As}_2$ with good cleavage planes (001) were synthesized using a self-flux technique [39,49]. The temperature dependence of the in-plane resistivity, shown in Fig. 1, was measured using a standard four-probe configuration using a Quantum Design physical property measurement system; the unit cell for the high-temperature tetragonal phase is shown in the inset. The resistivity decreases gradually with temperature, showing a weak inflection point at $T_{\rm N} \simeq 125$ K with a more pronounced decrease in the resistivity at $T_r \simeq 42$ K; the resistivity goes to zero below the superconducting transition at $T_c \simeq 10$ K. The reflectance from freshly cleaved surfaces was measured at a near-normal angle of incidence over a wide temperature (≃5 to 300 K) and frequency range (≃2 meV to about 5 eV) with Bruker IFS 113v and Vertex 80v Fourier transform spectrometers for light polarized in the *a*-*b* planes using an *in situ*

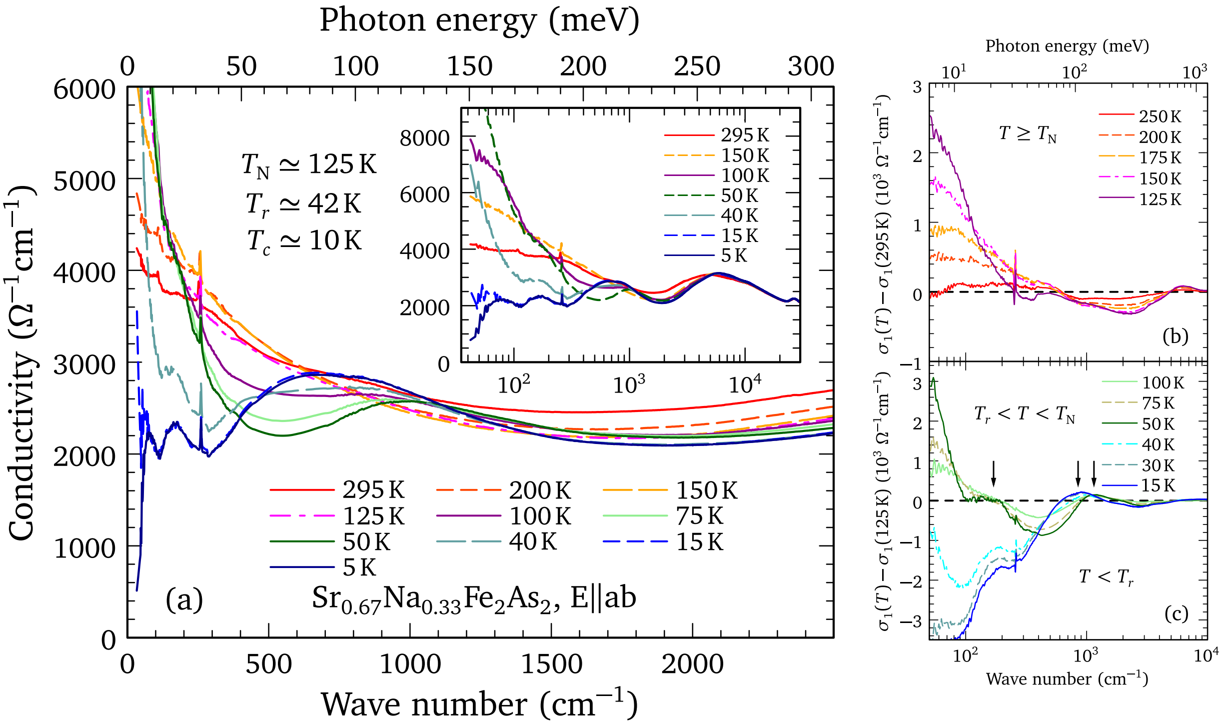

FIG. 2. (a) The temperature dependence of the real part of the optical conductivity of $Sr_{0.67}Na_{0.33}Fe_2As_2$ in the infrared region for light polarized in the Fe-As planes. Inset: The conductivity over a wide spectral range at several temperatures. (b) The $\sigma_1(\omega, T) - \sigma_1(\omega, 295\,K)$ difference plot for $T \geqslant T_N$ over a wide spectral range showing the narrowing of the free-carrier response and the transfer of spectral weight from high to low frequency. (c) The $\sigma_1(\omega, T) - \sigma_1(\omega, 125\,K)$ difference plot. In the $T_r < T < T_N$ region the free-carrier response continues to narrow, and a peak emerges in the midinfrared region. For $T < T_r$, the low-frequency conductivity is further suppressed, the midinfrared peak shifts to low energy, and a prominent peak is observed at $\simeq$170 cm^{-1} (arrows).

evaporation technique [50]. The complex optical properties were determined from a Kramers-Kronig analysis of the reflectivity. The reflectivity is shown in Fig. S1 in the Supplemental Material; the details of the Kramers-Kronig analysis are also described in the Supplemental Material [51]. Temperature-dependent ARPES measurements were performed to track the evolution of the electron and hole pockets in the various phases. Measurements at BNL, which focused on the electronic structure near the center of the Brillouin zone, were performed using 21.2-eV light from a monochromator-filtered He I source (Omicron VUV5k) and a Scienta SES-R4000 electron spectrometer; emitted electrons were collected along the direction perpendicular to the light-surface mirror plane. Samples were cleaved at low temperature and measured in an ultrahigh vacuum with a base pressure better than 5×10^{-10} mbar. Measurements at the National Laboratory for Superconductivity, Institute of Physics, Chinese Academy of Sciences, were performed using a 21.2-eV helium discharge lamp and a Scienta DA30L electron spectrometer. The latter's overall energy resolution was 10 meV for Fermi surface mapping and 4 meV for the cuts; the angular resolution was ~0.1°. All the samples were cleaved at low temperature and measured in an ultrahigh vacuum with a base pressure better than 5×10^{-11} mbar. Note that because uniaxial strain is not applied to the samples below T_N, they will be heavily twinned; thus, the optical and ARPES results represent an average of the *a* and *b* axis response in the magnetic C_2 phase.

III. RESULTS AND DISCUSSION

A. Optical properties

The temperature dependence of the real part of the in-plane optical conductivity $\sigma_1(\omega)$ of $Sr_{0.67}Na_{0.33}Fe_2As_2$ is shown in the infrared region in Fig. 2(a) (an additional plot of the optical conductivity is shown in Fig. S2). The character of the conductivity changes dramatically through the structural and magnetic transitions, which can be characterized by four distinct regions: (i) $T > T_N$, (ii) $T_r < T < T_N$, (iii) $T < T_r$, and (iv) below the superconducting transition, $T < T_c$. The changes in the nature of the conductivity are shown as the difference plots $\sigma_1(\omega, T) - \sigma_1(\omega, 295\,K)$ and $\sigma_1(\omega, T) - \sigma_1(\omega, 125\,K)$, shown in Figs. 2(b) and 2(c), respectively.

At room temperature, the free-carrier response appears Drude-like (a Lorentzian centered at zero frequency with a scattering rate defined as the full width at half maximum), giving way to a flat response at higher frequencies, until the first interband transitions are encountered at about 1 eV. As the temperature is reduced, the scattering rate decreases, and there is a slight reduction of the conductivity in the midinfrared region as spectral weight is transferred from high to low frequency, which leads to an increase at low frequency and a decrease at high frequency in the difference spectra in Fig. 2(b). Below T_N in the C_2 phase, the free-carrier response narrows dramatically, and a peaklike structure emerges at about 950 cm^{-1}, somewhat lower than a similar feature that was observed below T_N at $\simeq$1400 cm^{-1} in the parent

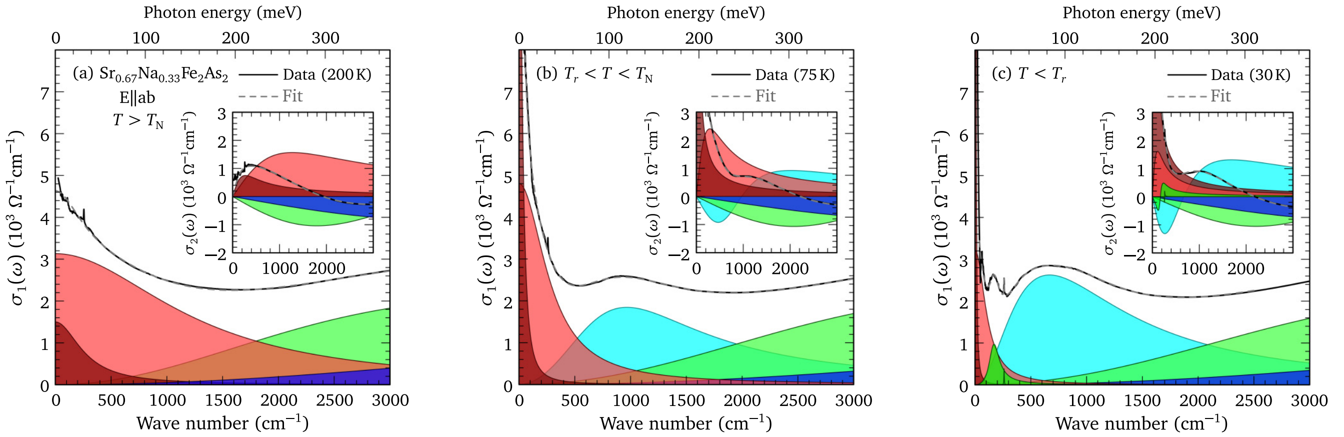

FIG. 3. The Drude-Lorentz model fits to the real and imaginary (inset) parts of the in-plane optical conductivity of $Sr_{0.67}Na_{0.33}Fe_2As_2$ decomposed into the narrow (D1) and broad (D2) Drude components, as well as several bound excitations (a) above T_N at 200 K, (b) below T_N at 75 K, showing the narrowing of the Drude features and the emergence of a peak at $\simeq$950 cm^{-1}, and (c) below T_r at 30 K, showing further narrowing and peaks at $\simeq$170 and 700 cm^{-1}.

compound $SrFe_2As_2$ [52]. This is illustrated by the upper three curves in Fig. 2(c) that show the continuing increase in the low-frequency conductivity, as well as the emergence of a peak in the midinfrared region. Interestingly, below $\simeq$75 K, a low-energy peak at $\simeq$170 cm^{-1} begins to emerge. This behavior continues until $T \leqslant T_r$, at which point the Drude-like response becomes extremely narrow in the C_4 phase, illustrated by the dramatic suppression of the low-frequency conductivity in the difference plot in Fig. 2(c), leaving clearly identifiable peaks at $\simeq$170 and 700 cm^{-1}. Below $T_c \simeq 10$ K, there is a depletion of the low-frequency conductivity with the emergence of a shoulderlike structure around 70 cm^{-1} that signals the formation of a superconducting energy gap (Fig. S2).

The sharp feature observed in the conductivity at $\simeq$260 cm^{-1} is attributed to a normally infrared-active lattice vibration in the iron-arsenic planes; while this mode increases in frequency with decreasing temperature, it does not display the anomalous increase in oscillator strength below T_N that was observed in the parent compound [53]. However, below T_r there is evidence for a new satellite mode appearing at $\simeq$282 cm^{-1} (Fig. S3); a similar feature was also observed in the C_4 phase of $Ba_{1-x}K_xFe_2As_2$ and is attributed to Brillouin-zone folding due to the formation of a supercell in the CSDW phase [54].

Previous optical studies of the iron-arsenic materials recognized that these are multiband materials with hole and electron pockets at the center and corners of the Brillouin zone [55,56]; a minimal description consists of two electronic subsystems using the so-called two-Drude model [57]. The complex dielectric function $\tilde{\epsilon} = \epsilon_1 + i\epsilon_2$ can be written as

$$\tilde{\epsilon}(\omega) = \epsilon_\infty - \sum_{j=1}^{2} \frac{\omega_{p,D;j}^2}{\omega^2 + i\omega/\tau_{D,j}} + \sum_k \frac{\Omega_k^2}{\omega_k^2 - \omega^2 - i\omega\gamma_k}, \qquad (1)$$

where ϵ_∞ is the real part at high frequency. In the first sum, $\omega_{p,D;j}^2 = 4\pi n_j e^2/m_j^*$ and $1/\tau_{D,j}$ are the square of the plasma frequency and scattering rate for the delocalized (Drude) carriers in the jth band, respectively, and n_j and m_j^* are the carrier concentration and effective mass. In the second summation, ω_k, γ_k, and Ω_k are the position, width, and strength of the kth vibration or bound excitation. The complex conductivity is $\tilde{\sigma}(\omega) = \sigma_1 + i\sigma_2 = -2\pi i\omega[\tilde{\epsilon}(\omega) - \epsilon_\infty]/Z_0$ (in units of Ω^{-1}cm^{-1}); $Z_0 \simeq 377$ Ω is the impedance of free space. The model is fit to the real and imaginary parts of the optical conductivity simultaneously using a nonlinear least-squares technique. The results of the fits are shown in Figs. 3(a), 3(b), and 3(c) at 200 K ($T > T_N$), 75 K ($T_r < T < T_N$), and 30 K ($T < T_r$), respectively; the combined response has been decomposed into individual Drude and Lorentz components. In agreement with previous studies on the iron-based materials, the complex conductivity can be described by two Drude terms, one weak and narrow (D1) and the other strong and broad (D2), as well as several Lorentzian oscillators. The temperature dependence of the plasma frequencies, the D1 and D2 components, and the strength of the midinfrared (MIR) peak are shown in Fig. 4(a); the temperature dependence of the scattering rates for the two Drude components is shown in Fig. 4(b).

1. $T > T_N$

At room temperature, the plasma frequencies for the narrow and broad Drude terms, $\omega_{p,D1} \simeq 4400$ cm^{-1} and $\omega_{p,D2} \simeq 15\,800$ cm^{-1}, respectively, are slightly less than those of the undoped parent compound $SrFe_2As_2$ ($\omega_{p,D1} \simeq 5200$ cm^{-1} and $\omega_{p,D2} \simeq 17\,700$ cm^{-1}); however, the scattering rates of $1/\tau_{D1} \simeq 330$ cm^{-1} and $1/\tau_{D2} \simeq 1400$ cm^{-1} are noticeably lower than the values of $1/\tau_{D1} \simeq 470$ cm^{-1} and $1/\tau_{D2} \simeq 2330$ cm^{-1} observed in the undoped material [52]. This is somewhat surprising considering that in this material the layers in between the Fe-As sheets are disordered. While the plasma frequencies show little temperature dependence between room temperature and T_N, the scattering rates for both Drude components decrease with temperature, with the narrow Drude decreasing from about $1/\tau_{D1} \simeq 330$ to about

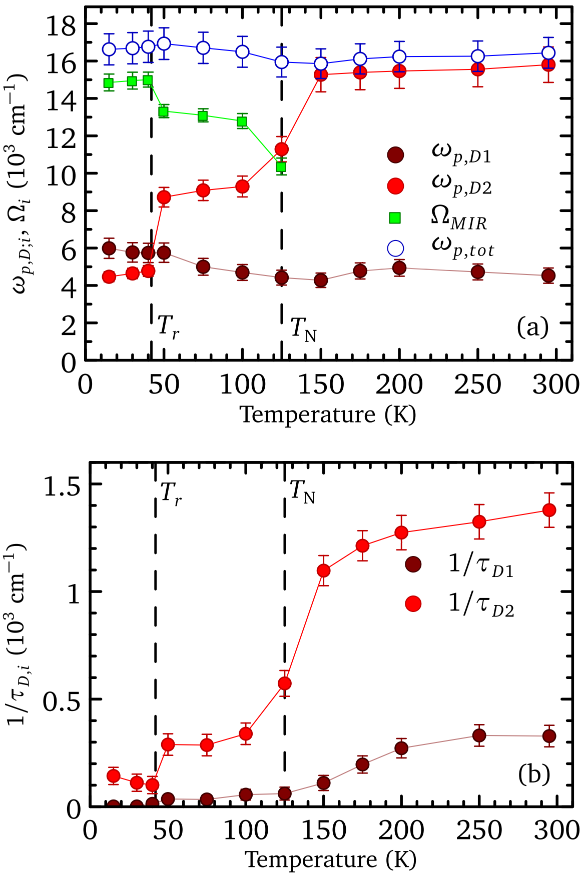

FIG. 4. (a) The temperature dependence of the plasma frequencies of the narrow (D1) and broad (D2) Drude components, the oscillator strength of the midinfrared peak $\Omega_{\rm MIR}$, and the total when these three components are added in quadrature $\omega_{p,\rm tot}$ for $\rm Sr_{0.67}Na_{0.33}Fe_2As_2$. (b) The temperature dependence of the scattering rates of the narrow and broad Drude components.

60 cm^{-1} and the broad Drude decreasing from $1/\tau_{D2} \simeq$ 1400 cm^{-1} to about 1100 cm^{-1} just above $T_{\rm N}$.

2. $T_r < T < T_{\rm N}$

Below $T_{\rm N}$ in the magnetic C_2 phase, the plasma frequency for the narrow Drude increases slightly from $\omega_{p,D1} \simeq 4400$ to $\simeq 6000$ cm^{-1}, while the scattering rate continues to decrease to $1/\tau_{D1} \simeq 40$ cm^{-1} just above T_r. The broad Drude displays much larger changes, with the plasma frequency decreasing from $\omega_{p,D2} \simeq 15\,800$ to 9000 cm^{-1}, which corresponds to a decrease in carrier concentration of nearly 65% ($\omega_p^2 \propto n/m^*$); the scattering rate also drops dramatically from $1/\tau_{D2} \simeq$ 1100 cm^{-1} just above $T_{\rm N}$ to 300 cm^{-1} in the $T_r < T < T_{\rm N}$ region. The dramatic loss of spectral weight of the broad Drude term is accompanied by the emergence of a new peak in the MIR region with position $\omega_{\rm MIR} \simeq 950$ cm^{-1}, width $\gamma_{\rm MIR} \simeq$ 1550 cm^{-1}, and strength $\Omega_{\rm MIR} \simeq 13\,000$ cm^{-1} [Fig. 3(b)]; the missing weight from the free carriers is transferred into this bound excitation, and accordingly, the total spectral weight is defined as $\omega_{p,\rm tot}^2 = \omega_{p,D1}^2 + \omega_{p,D2}^2 + \Omega_{\rm MIR}^2$ and is constant, as shown in Fig. 4(a). This behavior is similar to what was previously observed in the parent compound and has been explained as the partial gapping of the pocket responsible for the broad Drude term and the appearance of a low-energy interband transition [52,58].

3. $T < T_r$

As the temperature is reduced, the system undergoes a further magnetic and structural transition at $T_r \simeq 42$ K and enters the magnetic C_4 phase. Below T_r the plasma frequency for the narrow Drude term appears to actually increase slightly. However, this is accompanied by a dramatic collapse of $1/\tau_{D1} \simeq$ 40 cm^{-1} just above T_r to a value of $\simeq$2 cm^{-1} at 15 K; this is nearly an order of magnitude smaller than what is observed in the parent compound [52]. Consequently, the narrow Drude is no longer observable in $\sigma_1(\omega)$, leaving a relatively flat optical conductivity due to the broad Drude term and Lorentzian components; instead, its effects are determined from $\sigma_2(\omega)$ [shown in the inset of Fig. 3(c)]. The plasma frequency of the broad Drude term continues to decrease from $\omega_{p,D2} \simeq 9000$ to about 4200 cm^{-1} at 15 K, a further 80% reduction in the carrier concentration associated with this pocket and over 90% from the room temperature value; this is comparable to what was observed in the parent compound for $T \ll T_{\rm N}$ [52]. In addition, the scattering rate decreases from $1/\tau_{D2} \simeq 300$ cm^{-1} at T_r to $\simeq$120 cm^{-1} at 15 K. At the same time, the peak at $\omega_{\rm MIR} \simeq 950$ cm^{-1} shifts down to about $\simeq$650 cm^{-1}; while the width decreases slightly to $\gamma_{\rm MIR} \simeq 1480$ cm^{-1}, the strength of this feature increases to $\Omega_{\rm MIR} \simeq 15\,400$ cm^{-1}. However, $\omega_{p,\rm tot}$ continues to be conserved, indicating that the loss of spectral weight associated with the free carriers in the broad Drude term has been transferred to this peak.

4. $T < T_c$

Below $T_c \simeq 10$ K there is a dramatic suppression of the low-frequency conductivity, signaling the formation of a superconducting energy gap [Figs. 2(a) and S2]. Although the low-frequency data are somewhat limited, a comparison of the optical conductivities for $T \gtrsim T_c$ and $T \ll T_c$ allows the superfluid density, $\rho_s = \omega_{ps}^2$, where ω_{ps} is the superconducting plasma frequency, to be determined from the missing spectral weight, calculated using the Ferrell-Glover-Tinkham (FGT) sum rule [59,60]. The FGT sum rule converges to $\omega_{ps} \simeq 5800 \pm 500$ cm^{-1}, which corresponds to a superconducting penetration depth of $\lambda \simeq 2700 \pm 300$ Å at 5 K, comparable to the K-doped material [47]; however, because the lowest temperature obtained was only $\simeq T_c/2$, it is almost certain that ω_{ps} is underestimated. From Figs. 2(a) and S2, the characteristic energy scale for the superconducting energy gap is about $2\Delta \simeq 50$ cm^{-1}. In the narrow Drude band, $1/\tau_{D1} \ll 2\Delta$, placing this material in the clean limit; as a result, most of the weight in the condensate will come from this band. In the broad Drude band, $1/\tau_{D2} > 2\Delta$, placing this band in the dirty limit; consequently, only a small fraction of the weight in this band will collapse into the condensate. This is another example of a multiband iron-based superconductor that is simultaneously in both the clean and dirty limits [61]. One of the interesting properties of this material is its relatively low resistivity just above T_c, $\rho_{ab} \simeq 20$ $\mu\Omega$ cm, or $\sigma_{\rm dc} \simeq 5 \times 10^4$ Ω^{-1} cm^{-1} (Fig. 1). These values place this material just below the universal scaling line $\rho_s(T \ll T_c) \propto$

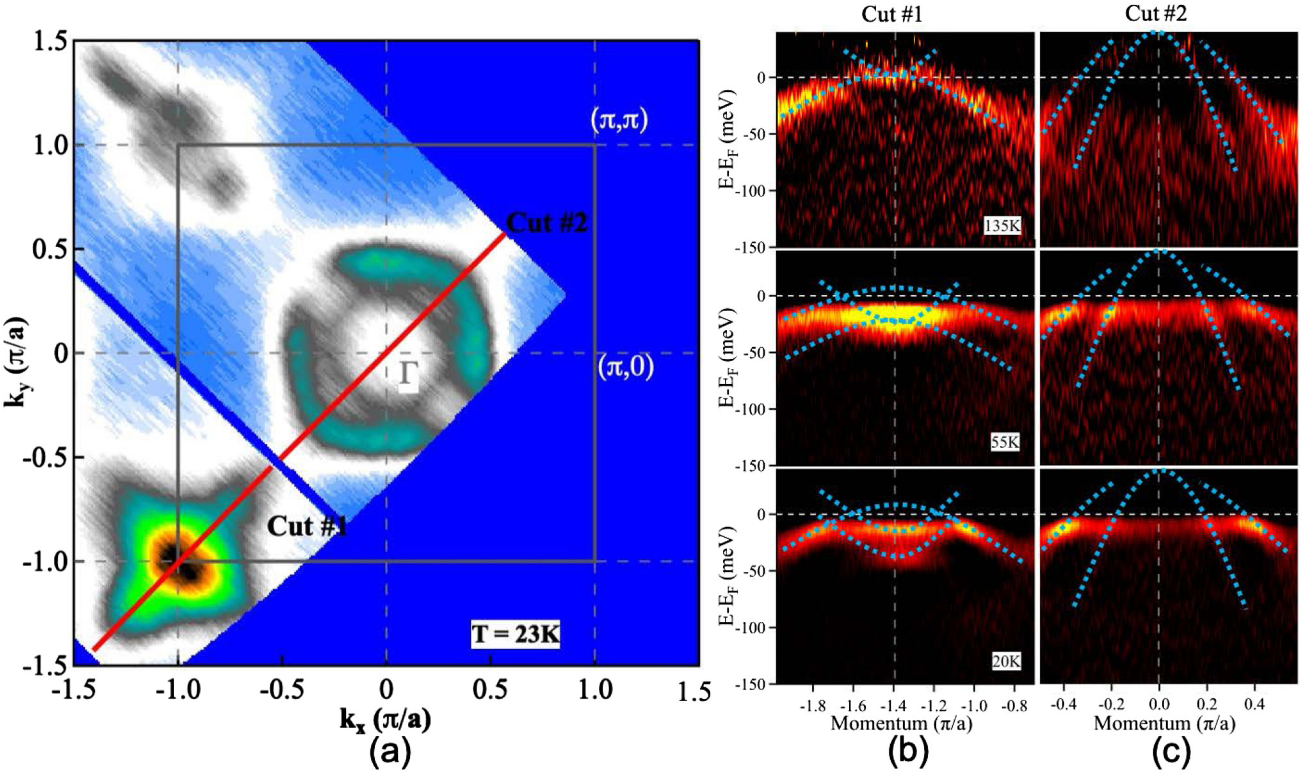

FIG. 5. (a) Fermi surface mapping of $Sr_{0.67}Na_{0.33}Fe_2As_2$ in the C_4 magnetic phase at 23 K with the spectral weight integrated within a ±10-meV energy window with respect to the Fermi level, showing the holelike pockets at the center (Γ) and the electronlike pockets at the corner (M) of the Brillouin zone. Several different cuts are shown along the $\Gamma \rightarrow M$ path focus on the evolution of the hole and electron pockets. (b) The temperature dependence of the second derivative of the energy bands measured along the first cut around the M point at $(-\pi, -\pi)$ at 135 K ($T > T_N$), 55 K ($T_r < T < T_N$), and 20 K ($T_c < T < T_r$). (c) The temperature dependence of the second derivative of the energy bands measured along the second cut around the Γ point at 135, 55, and 20 K. The dotted lines are drawn as a guide to the eye.

$\sigma_{dc}(T \gtrsim T_c)\, T_c$ [62–64], in close proximity to other doped 122 superconductors, as well as many cuprate materials [65].

B. Low-energy peak

The dramatic collapse of the scattering rate below T_r of the narrow Drude allows a new low-energy peak at $\omega_0 \simeq 170\ \text{cm}^{-1}$, with width $\gamma_0 \simeq 110\ \text{cm}^{-1}$ and an oscillator strength of $\Omega_0 \simeq 2230\ \text{cm}^{-1}$, to be observed [Figs. 2(a), 3(c), and S2]. This is close to where a peak was observed in $(CaFe_{1-x}Pt_xAs)_{10}Pt_3As_8$ for $x = 0.1$ at $\simeq 120\ \text{cm}^{-1}$ [66]; that feature was attributed to a localization process due to impurity scattering described by a classical generalization of the Drude model [67],

$$\tilde{\sigma}(\omega) = \left(\frac{2\pi}{Z_0}\right)\frac{\omega_p^2\tau}{(1-i\omega\tau)}\left[1+\frac{c}{(1-i\omega\tau)}\right], \qquad (2)$$

where c is the persistence of velocity that is retained for a single collision. The scattering rate for the narrow Drude is far too small to yield a peak at the experimentally observed position, while the broad Drude predicts a localization peak at $\simeq 120\ \text{cm}^{-1}$, well below the experimentally observed value of $\omega_0 \simeq 170\ \text{cm}^{-1}$ [68]. Thus, it is likely that the low-energy peak originates from a further reconstruction of the Fermi surface in the C_4 phase rather than any sort of localization process. Indeed, a remarkably similar peak was also observed to emerge at $\simeq 150\ \text{cm}^{-1}$ in the optical conductivity of underdoped $Ba_{1-x}K_xFe_2As_2$ at low temperature [69]; this feature may also be a related to the magnetic C_4 phase observed in that compound.

C. ARPES

A simple density functional theory calculation of $SrFe_2As_2$ in the paramagnetic high-temperature tetragonal phase reveals a familiar band structure consisting of three holelike pockets at the center of the Brillouin zone (Γ) and two electronlike pockets at the corners (M); the orbital character is primarily Fe d_{xz}/d_{yz} in nature (shown in Fig. S4; details of the calculation are discussed in the Supplemental Material.) The Fermi surface of $Sr_{0.67}Na_{0.33}Fe_2As_2$, with the spectral weight integrated within a ±10-meV energy window with respect to the Fermi level, is shown below T_r in the C_4 magnetic phase at 23 K in Fig. 5(a). Two momentum cuts have been made along the $\Gamma \rightarrow M$ path; the first examines the temperature dependence of the anisotropic electronlike bands around an M point [Fig. 5(b)], and the second details the behavior of the isotropic holelike pockets around the Γ point, shown in Fig. 5(c). This Fermi surface is qualitatively similar to what was observed in $Ba_{1-x}K_xFe_2As_2$ [70,71] 4

At high temperature, at the cut along the $\Gamma \rightarrow M$ direction at the M point there appears to be a holelike band as well as a possible electronlike band at 135 K, shown in the top panel of Fig. 5(b). In the simple picture for the Fermi surface of

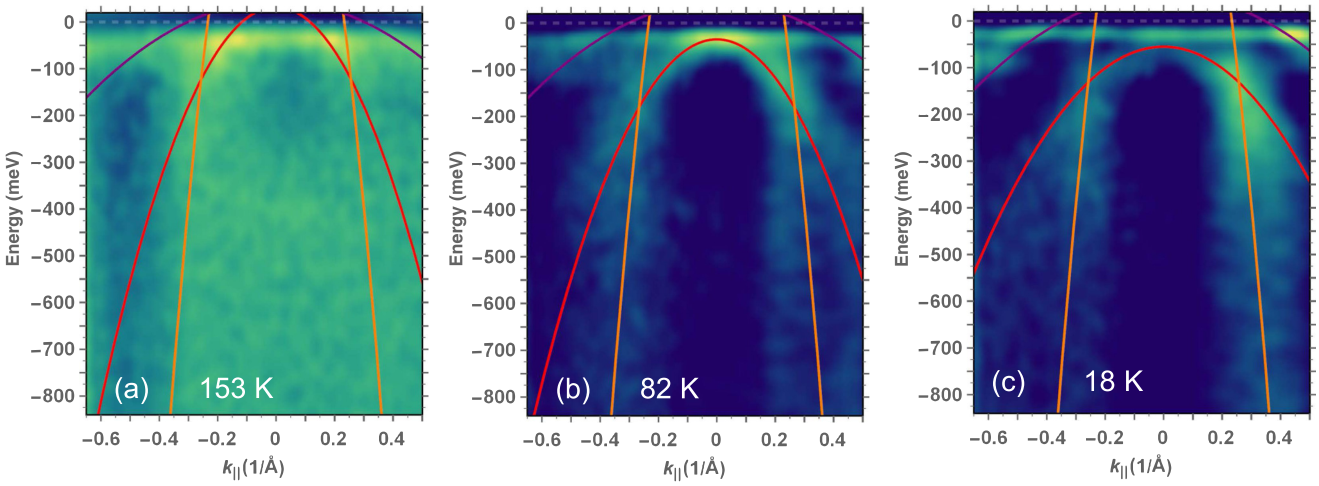

FIG. 6. The temperature dependence of the second derivative of the holelike bands of $Sr_{0.67}Na_{0.33}Fe_2As_2$ around the Γ point along the $\Gamma \rightarrow M$ cut (a) above T_N at 153 K, (b) for $T_r < T < T_N$ at 82 K, and (c) below T_r at 18 K. At high temperature three holelike bands may be resolved that cross ϵ_F. Below T_N two of these bands shift to below the Fermi level; this trend continues below T_r as the bands shift further below ϵ_F. The lines are drawn as a guide to the eye.

$SrFe_2As_2$ (Fig. S4) this result can be reproduced by lowering the Fermi level ϵ_F by about 0.2 eV, which is consistent with the removal of electrons due to sodium substitution (hole doping). As the temperature is lowered below T_N and enters the magnetic C_2 phase, the holelike band may split, while the electronlike band appears to shift below ϵ_F. Below T_r in the C_4 magnetic phase, a single holelike band is recovered, while the electronlike band now appears to be split into two bands, with a separation of $\simeq$20 meV, which is comparable to the position of the low-energy peak (this behavior is explored further in Fig. S5).

The initial investigation into the temperature dependence of the energy bands around the Γ point in Fig. 5(c) revealed two large hole pockets at the Fermi level but relatively little temperature dependence. This prompted a more detailed investigation of the holelike bands along the $\Gamma \rightarrow M$ path, shown in Fig. 6 (further detail is provided in Figs. S6 and S7). Above T_N the bands are rather broad, but at least three bands may be resolved, all of which cross the Fermi level, resulting in several large holelike Fermi surfaces, shown in the second-derivative curves in Fig. 6(a). Below T_N the bands sharpen considerably in the C_2 phase, and one of the bands is observed to shift to $\simeq$40 meV below the Fermi level, shown in Fig. 6(b), leading to the removal of a holelike Fermi surface; this is consistent with the Fermi surface reconstruction below T_N observed in the parent compounds [58,72]. This trend continues in the magnetic C_4 phase, with the band shifting to $\simeq$60 meV below the Fermi level [Fig. 6(c)].

D. Discussion

Both the electron and hole pockets appear to undergo significant changes in response to the Fermi surface reconstruction in the magnetic C_2 and C_4 phases that exhibit SDW and CSDW order, respectively. In the case of the hole pockets, the fact that one of the bands shifts below ϵ_F below T_N in the magnetic C_2 phase, shifting further below T_r in the magnetic C_4 phase, signals the decrease in the size of the Fermi surface associated with the hole pockets. It is possible that this may be related to the dramatic decrease in the spectral weight of the broad Drude component as described by the plasma frequency in Fig. 4(a); from $\omega_{p,D2}^2 \propto n/m^*$ we infer a significant decrease in the carriers associated with the hole pockets at low temperature ($\simeq$90% reduction of the room temperature value).

The evolution of the electronlike bands is more complicated, as the bands at the M point have both electron- and holelike character. The initial splitting of the holelike band below T_N is consistent with the lifting of the degeneracy between the d_{xz} and d_{yz} orbitals; however, the fact that one of the holelike bands lies completely below the Fermi level suggests no significant changes to the size of the Fermi surfaces. Below T_r the orbital degeneracy is restored, but the presence of CSDW order leads to the formation of a supercell; the electronlike bands are split as a result of zone folding, which may lead to an increase in the size of the Fermi surface. This is consistent with the slight increase in the plasma frequency of the narrow Drude component at low temperature, shown in Fig. 4(a). Furthermore, the splitting between the two electronlike bands of $\simeq$20 meV is very close to the position of the low-energy peak. This suggests that, similar to the midinfrared peak, the low-energy peak emerges in response to the Fermi surface reconstruction driven by the C_4 magnetic phase and the CSDW order at low temperature [43].

IV. SUMMARY

The ARPES and complex optical properties of freshly cleaved surfaces of the iron-based superconductor $Sr_{0.67}Na_{0.33}Fe_2As_2$ have been determined for light polarized in the iron-arsenic (a-b) planes at a variety of temperatures for the room temperature tetragonal paramagnetic phase, the orthorhombic C_2 SDW magnetic phase, and the tetragonal C_4 double-**Q** SDW (CSDW) phase, as well as below T_c in the superconducting state. The free-carrier response is described by two Drude components, one broad and strong and the other narrow and weak. The strength of the narrow component shows little temperature dependence, increasing slightly in strength at low temperature, while narrowing dramatically. The broad Drude component decreases dramatically in strength and narrows below T_N at the same time a peak emerges in the midinfrared; the decrease in the spectral weight associated with the free carriers is transferred into the emergent peak. Below T_r, this trend continues, with the emergence of a new low-energy peak at $\simeq$20 meV. The appearance of a new infrared-active mode in the Fe-As planes below T_r is attributed to zone folding due to the formation of a supercell in response to the CSDW; this suggests that the low-energy peak originates from a further Fermi surface reconstruction in the C_4 phase. Below T_c the low-frequency conductivity decreases dramatically, signaling the formation of a superconducting energy gap. ARPES reveals large holelike Fermi surfaces at the Γ point, one of which is apparently removed below the structural and magnetic transitions, suggesting that they may be related to the behavior of the broad Drude component. The electron- and holelike bands at the corners of the Brillouin zone shift and split below T_N and T_r, but the Fermi surfaces do not appear to undergo any significant change in size, suggesting they may be related to the narrow Drude component; the apparent splitting of the electronlike bands in the C_4 phase would appear to explain the emergence of the low-energy peak at $\simeq$20 meV in the optical conductivity. While the C_2 and C_4 magnetic transitions, with resulting SDW and CSDW order, respectively, lead to a significant reconstruction of the Fermi surface that has profound implications for the transport originating from the electron- and holelike pockets, they appear to have relatively little impact on the superconductivity in this material.

ACKNOWLEDGMENTS

Work at the Chinese Academy of Science was supported by NSFC (Projects No. 11774400, No. 11888101, and No. 11974412) and MOST (Projects No. 2015CB921102, No. 2016YFA0300300, and No. 2017YFA0302903). Work at HPSTAR was supported by NSAF, Grant No. U1530402. Work at Brookhaven National Laboratory was supported by the Office of Science, US Department of Energy, under Contract No. DE-SC0012704. FQ

---

[1] D. C. Johnston, The puzzle of high temperature superconductivity in layered iron pnictides and chalcogenides, Adv. Phys. **59**, 803 (2010).

[2] J. Paglione and R. L. Greene, High-temperature superconductivity in iron-based materials, Nat. Phys. **6**, 645 (2010).

[3] P. C. Canfield and S. L. Bud'ko, FeAs-based superconductivity: A case study of the effects of transition metal doping on $BaFe_2As_2$, Annu. Rev. Condens. Matter Phys. **1**, 27 (2010).

[4] Q. Si, R. Yu, and E. Abrahams, High-temperature superconductivity in iron pnictides and chalcogenides, Nat. Rev. Mater. **1**, 16017 (2016).

[5] M. P. M. Dean, M. G. Kim, A. Kreyssig, J. W. Kim, X. Liu, P. J. Ryan, A. Thaler, S. L. Bud'ko, W. Strassheim, P. C. Canfield, J. P. Hill, and A. I. Goldman, Magnetically polarized Ir dopant atoms in superconducting $Ba(Fe_{1-x}Ir_x)_2As_2$, Phys. Rev. B **85**, 140514(R) (2012).

[6] P. Dai, Antiferromagnetic order and spin dynamics in iron-based superconductors, Rev. Mod. Phys. **87**, 855 (2015).

[7] M. Moroni, P. Carretta, G. Allodi, R. De Renzi, M. N. Gastiasoro, B. M. Andersen, P. Materne, H.-H. Klauss, Y. Kobayashi, M. Sato, and S. Sanna, Fast recovery of the stripe magnetic order by Mn/Fe substitution in F-doped LaFeAsO superconductors, Phys. Rev. B **95**, 180501(R) (2017).

[8] A. Kreyssig, J. M. Wilde, A. E. Böhmer, W. Tian, W. R. Meier, B. Li, B. G. Ueland, M. Xu, S. L. Bud'ko, P. C. Canfield, R. J. McQueeney, and A. I. Goldman, Antiferromagnetic order in $CaK(Fe_{1-x}Ni_x)_4As_4$ and its interplay with superconductivity, Phys. Rev. B **97**, 224521 (2018).

[9] W. R. Meier, Q.-P. Ding, A. Kreyssig, S. L. Bud'ko, A. Sapkota, K. Kothapalli, V. Borisov, R. Valentí, C. D. Batista, P. P. Orth, R. M. Fernandes, A. I. Goldman, Y. Furukawa, A. E. Böhmer, and P. C. Canfield, Hedgehog spin-vortex crystal stabilized in a hole-doped iron-based superconductor, npj Quantum Mater. **3**, 5 (2018).

[10] M. Rotter, M. Tegel, and D. Johrendt, Superconductivity at 38 K in the Iron Arsenide $(Ba_{1-x}K_x)Fe_2As_2$, Phys. Rev. Lett. **101**, 107006 (2008).

[11] A. S. Sefat, R. Jin, M. A. McGuire, B. C. Sales, D. J. Singh, and D. Mandrus, Superconductivity at 22 K in Co-Doped $BaFe_2As_2$ Crystals, Phys. Rev. Lett. **101**, 117004 (2008).

[12] N. Ni, M. E. Tillman, J.-Q. Yan, A. Kracher, S. T. Hannahs, S. L. Bud'ko, and P. C. Canfield, Effects of Co substitution on thermodynamic and transport properties and anisotropic H_{c2} in $Ba(Fe_{1-x}Co_x)_2As_2$ single crystals, Phys. Rev. B **78**, 214515 (2008).

[13] K. Sasmal, B. Lv, B. Lorenz, A. M. Guloy, F. Chen, Y.-Y. Xue, and C.-W. Chu, Superconducting Fe-Based Compounds $(A_{1-x}Sr_x)Fe_2As_2$ with $A =$ K and Cs with Transition Temperatures up to 37 K, Phys. Rev. Lett. **101**, 107007 (2008).

[14] G.-F. Chen, Z. Li, G. Li, W.-Z. Hu, J. Dong, X.-D. Z. Jun Zhou, P. Zheng, N.-L. Wang, and J.-L. Luo, Superconductivity in hole-doped $(Sr_{1-x}K_x)Fe_2As_2$, Chin. Phys. Lett. **25**, 3403 (2008).

[15] J.-H. Chu, J. G. Analytis, C. Kucharczyk, and I. R. Fisher, Determination of the phase diagram of the electron-doped superconductor $Ba(Fe_{1-x}Co_x)_2As_2$, Phys. Rev. B **79**, 014506 (2009).

[16] T. Goko, A. A. Aczel, E. Baggio-Saitovitch, S. L. Bud'ko, P. C. Canfield, J. P. Carlo, G. F. Chen, P. Dai, A. C. Hamann, W. Z. Hu, H. Kageyama, G. M. Luke, J. L. Luo, B. Nachumi, N. Ni, D. Reznik, D. R. Sanchez-Candela, A. T. Savici, K. J. Sikes, N. L. Wang, C. R. Wiebe, T. J. Williams, T. Yamamoto, W. Yu, and Y. J. Uemura, Superconducting state coexisting

with a phase-separated static magnetic order in (Ba,K)Fe_2As_2, (Sr,Na)Fe_2As_2, and $CaFe_2As_2$, Phys. Rev. B **80**, 024508 (2009).

[17] S. R. Saha, N. P. Butch, K. Kirshenbaum, and J. Paglione, Evolution of bulk superconductivity in $SrFe_2As_2$ with Ni substitution, Phys. Rev. B **79**, 224519 (2009).

[18] S. Jiang, H. Xing, G. Xuan, C. Wang, Z. Ren, C. Feng, J. Dai, Z. Xu, and G. Cao, Superconductivity up to 30 K in the vicinity of the quantum critical point in $BaFe_2(As_{1-x}P_x)_2$, J. Phys.: Condens. Matter **21**, 382203 (2009).

[19] H. L. Shi, H. X. Yang, H. F. Tian, J. B. Lu, Z. W. Wang, Y. B. Qin, Y. J. Song, and J. Q. Li, Structural properties and superconductivity of $SrFe_2As_{2-x}P_x$ and $(0.0 \leqslant x \leqslant 1.0)$ and $CaFe_2As_{2-y}P_y$ $(0.0 \leqslant y \leqslant 0.3)$, J. Phys.: Condens. Matter **22**, 125702 (2010).

[20] R. Cortes-Gil and S. J. Clarke, Structure, Magnetism, and Superconductivity of the Layered Iron Arsenides $Sr_{1-x}Na_xFe_2As_2$, Chem. Mater. **23**, 1009 (2011).

[21] F. Ishikawa, N. Eguchi, M. Kodama, K. Fujimaki, M. Einaga, A. Ohmura, A. Nakayama, A. Mitsuda, and Y. Yamada, Zero-resistance superconducting phase in $BaFe_2As_2$ under high pressure, Phys. Rev. B **79**, 172506 (2009).

[22] P. L. Alireza, Y. T. C. Ko, J. Gillett, C. M. Petrone, J. M. Cole, S. E. Sebastian, and G. G. Lonzarich, Superconductivity up to 29 K in $SrFe_2As_2$ and $BaFe_2As_2$ at high pressures, J. Phys. Condens. Matter **21**, 012208 (2009).

[23] E. Colombier, S. L. Bud'ko, N. Ni, and P. C. Canfield, Complete pressure-dependent phase diagrams for $SrFe_2As_2$ and $BaFe_2As_2$, Phys. Rev. B **79**, 224518 (2009).

[24] K. Kitagawa, N. Katayama, H. Gotou, T. Yagi, K. Ohgushi, T. Matsumoto, Y. Uwatoko, and M. Takigawa, Spontaneous Formation of a Superconducting and Antiferromagnetic Hybrid State in $SrFe_2As_2$ under High Pressure, Phys. Rev. Lett. **103**, 257002 (2009).

[25] M. Tegel, M. Rotter, V. Weiß, F. M. Schappacher, R. Pöttgen, and D. Johrendt, Structural and magnetic phase transitions in the ternary iron arsenides $SrFe_2As_2$ and $EuFe_2As_2$, J. Phys.: Condens. Matter **20**, 452201 (2008).

[26] J.-Q. Yan, A. Kreyssig, S. Nandi, N. Ni, S. L. Bud'ko, A. Kracher, R. J. McQueeney, R. W. McCallum, T. A. Lograsso, A. I. Goldman, and P. C. Canfield, Structural transition and anisotropic properties of single-crystalline $SrFe_2As_2$, Phys. Rev. B **78**, 024516 (2008).

[27] J. Zhao, W. Ratcliff, J. W. Lynn, G. F. Chen, J. L. Luo, N. L. Wang, J. Hu, and P. Dai, Spin and lattice structures of single-crystalline $SrFe_2As_2$, Phys. Rev. B **78**, 140504(R) (2008).

[28] W. Z. Hu, J. Dong, G. Li, Z. Li, P. Zheng, G. F. Chen, J. L. Luo, and N. L. Wang, Origin of the Spin Density Wave Instability in AFe_2As_2 (A= Ba, Sr) as Revealed by Optical Spectroscopy, Phys. Rev. Lett. **101**, 257005 (2008).

[29] J. N. Hancock, S. I. Mirzaei, J. Gillett, S. E. Sebastian, J. Teyssier, R. Viennois, E. Giannini, and D. van der Marel, Strong coupling to magnetic fluctuations in the charge dynamics of iron-based superconductors, Phys. Rev. B **82**, 014523 (2010).

[30] E. C. Blomberg, M. A. Tanatar, A. Kreyssig, N. Ni, A. Thaler, R. Hu, S. L. Bud'ko, P. C. Canfield, A. I. Goldman, and R. Prozorov, In-plane anisotropy of electrical resistivity in strain-detwinned $SrFe_2As_2$, Phys. Rev. B **83**, 134505 (2011).

[31] M. A. Tanatar, A. Kreyssig, S. Nandi, N. Ni, S. L. Bud'ko, P. C. Canfield, A. I. Goldman, and R. Prozorov, Direct imaging of the structural domains in the iron pnictides AFe_2As_2(A = Ca, Sr, Ba), Phys. Rev. B **79**, 180508(R) (2009).

[32] I. R. Fisher, L. Degiorgi, and Z. X. Shen, In-plane electronic anisotropy of underdoped '122' Fe-arsenide superconductors revealed by measurements of detwinned single crystals, Rep. Prog. Phys. **74**, 124506 (2011).

[33] A. I. Goldman, D. N. Argyriou, B. Ouladdiaf, T. Chatterji, A. Kreyssig, S. Nandi, N. Ni, S. L. Bud'ko, P. C. Canfield, and R. J. McQueeney, Lattice and magnetic instabilities in $CaFe_2As_2$: A single-crystal neutron diffraction study, Phys. Rev. B **78**, 100506(R) (2008).

[34] M. Kofu, Y. Qiu, W. Bao, S.-H. Lee, S. Chang, T. Wu, G. Wu, and X. H. Chen, Neutron scattering investigation of the magnetic order in single crystalline $BaFe_2As_2$, New J. Phys. **11**, 055001 (2009).

[35] M. G. Kim, A. Kreyssig, A. Thaler, D. K. Pratt, W. Tian, J. L. Zarestky, M. A. Green, S. L. Bud'ko, P. C. Canfield, R. J. McQueeney, and A. I. Goldman, Antiferromagnetic ordering in the absence of structural distortion in $Ba(Fe_{1-x}Mn_x)_2As_2$, Phys. Rev. B **82**, 220503(R) (2010).

[36] E. Hassinger, G. Gredat, F. Valade, S. R. de Cotret, A. Juneau-Fecteau, J.-Ph. Reid, H. Kim, M. A. Tanatar, R. Prozorov, B. Shen, H.-H. Wen, N. Doiron-Leyraud, and L. Taillefer, Pressure-induced Fermi-surface reconstruction in the iron-arsenide superconductor $Ba_{1-x}K_xFe_2As_2$: Evidence of a phase transition inside the antiferromagnetic phase, Phys. Rev. B **86**, 140502(R) (2012).

[37] A. E. Böhmer, F. Hardy, L. Wang, T. Wolf, P. Schweiss, and C. Meingast, Superconductivity-induced re-entrance of the orthorhombic distortion in $Ba_{1-x}K_xFe_2As_2$, Nat. Commun. **6**, 7911 (2015).

[38] L. Wang, F. Hardy, A. E. Böhmer, T. Wolf, P. Schweiss, and C. Meingast, Complex phase diagram of $Ba_{1-x}Na_xFe_2As_2$: A multitude of phases striving for the electronic entropy, Phys. Rev. B **93**, 014514 (2016).

[39] K. M. Taddei, J. M. Allred, D. E. Bugaris, S. Lapidus, M. J. Krogstad, R. Stadel, H. Claus, D. Y. Chung, M. G. Kanatzidis, S. Rosenkranz, R. Osborn, and O. Chmaissem, Detailed magnetic and structural analysis mapping a robust magnetic C_4 dome in $Sr_{1-x}Na_xFe_2As_2$, Phys. Rev. B **93**, 134510 (2016).

[40] L. Wang, M. He, D. D. Scherer, F. Hardy, P. Schweiss, T. Wolf, M. Merz, B. M. Andersen, and C. Meingast, Competing Electronic Phases near the Onset of Superconductivity in Hole-Doped $SrFe_2As_2$, J. Phys. Soc. Jpn. **88**, 104710 (2019).

[41] E. Hassinger, G. Gredat, F. Valade, S. R. de Cotret, O. Cyr-Choinière, A. Juneau-Fecteau, J.-Ph. Reid, H. Kim, M. A. Tanatar, R. Prozorov, B. Shen, H.-H. Wen, N. Doiron-Leyraud, and L. Taillefer, Expansion of the tetragonal magnetic phase with pressure in the iron arsenide superconductor $Ba_{1-x}K_xFe_2As_2$, Phys. Rev. B **93**, 144401 (2016).

[42] K. M. Taddei, J. M. Allred, D. E. Bugaris, S. H. Lapidus, M. J. Krogstad, H. Claus, D. Y. Chung, M. G. Kanatzidis, R. Osborn, S. Rosenkranz, and O. Chmaissem, Observation of the magnetic C_4 phase in $Ca_{1-x}Na_xFe_2As_2$ and its universality in the hole-doped 122 superconductors, Phys. Rev. B **95**, 064508 (2017).

[43] M. Yi, A. Frano, D. H. Lu, Y. He, M. Wang, B. A. Frandsen, A. F. Kemper, R. Yu, Q. Si, L. Wang, M. He, F. Hardy, P. Schweiss, P. Adelmann, T. Wolf, M. Hashimoto, S.-K. Mo, Z. Hussain, M. Le Tacon, A. E. Böhmer, D.-H. Lee, Z.-X. Shen,

C. Meingast, and R. J. Birgeneau, Spectral Evidence for Emergent Order in $Ba_{1-x}Na_xFe_2As_2$, Phys. Rev. Lett. **121**, 127001 (2018).

[44] S. Avci, O. Chmaissem, J. M. Allred, S. Rosenkranz, I. Eremin, A. V. Chubukov, D. E. Bugaris, D. Y. Chung, M. G. Kanatzidis, J.-P Castellan, J. A. Schlueter, H. Claus, D. D. Khalyavin, P. Manuel, A. Daoud-Aladine, and R. Osborn, Magnetically driven suppression of nematic order in an iron-based superconductor, Nat. Commun. **5**, 3845 (2014).

[45] J. M. Allred, K. M. Taddei, D. E. Bugaris, M. J. Krogstad, S. H. Lapidus, D. Y. Chung, H. Claus, M. G. Kanatzidis, D. E. Brown, J. Kang, R. M. Fernandes, I. Eremin, S. Rosenkranz, O. Chmaissem, and R. Osborn, Double-Q spin-density wave in iron arsenide superconductors, Nat. Phys. **12**, 493 (2016).

[46] F. Waßer, A. Schneidewind, Y. Sidis, S. Wurmehl, S. Aswartham, B. Büchner, and M. Braden, Spin reorientation in $Ba_{0.65}Na_{0.35}Fe_2As_2$ studied by single-crystal neutron diffraction, Phys. Rev. B **91**, 060505(R) (2015).

[47] B. P. P. Mallett, Yu. G. Pashkevich, A. Gusev, Th. Wolf, and C. Bernhard, Muon spin rotation study of the magnetic structure in the tetragonal antiferromagnetic state of weakly underdoped $Ba_{1-x}K_xFe_2As_2$, Europhys. Lett. **111**, 57001 (2015).

[48] M. Hoyer, R. M. Fernandes, A. Levchenko, and J. Schmalian, Disorder-promoted C_4-symmetric magnetic order in iron-based superconductors, Phys. Rev. B **93**, 144414 (2016).

[49] J. Guo, L. Yue, K. Iida, K. Kamazawa, L. Chen, T. Han, Y. Zhang, and Y. Li, Preferred Magnetic Excitations in the Iron-Based $Sr_{1-x}Na_xFe_2As_2$ Superconductor, Phys. Rev. Lett. **122**, 017001 (2019).

[50] C. C. Homes, M. Reedyk, D. A. Crandles, and T. Timusk, Technique for measuring the reflectance of irregular, submillimeter-sized samples, Appl. Opt. **32**, 2976 (1993).

[51] See Supplemental Material at http://link.aps.org/supplemental/10.1103/PhysRevB.xx.xxxxxx for details of the experimental reflectivity and Kramers-Kronig analysis, which includes Refs. [73–77].

[52] Y. M. Dai, A. Akrap, S. L. Bud'ko, P. C. Canfield, and C. C. Homes, Optical properties of AFe_2As_2 (A = Ca, Sr, and Ba) single crystals, Phys. Rev. B **94**, 195142 (2016).

[53] C. C. Homes, Y. M. Dai, A. Akrap, S. L. Bud'ko, and P. C. Canfield, Vibrational anomalies in AFe_2As_2 (A = Ca, Sr, and Ba) single crystals, Phys. Rev. B **98**, 035103 (2018).

[54] B. P. P. Mallett, P. Marsik, M. Yazdi-Rizi, Th. Wolf, A. E. Böhmer, F. Hardy, C. Meingast, D. Munzar, and C. Bernhard, Infrared Study of the Spin Reorientation Transition and Its Reversal in the Superconducting State in Underdoped $Ba_{1-x}K_xFe_2As_2$, Phys. Rev. Lett. **115**, 027003 (2015).

[55] D. J. Singh, Electronic structure and doping in $BaFe_2As_2$ and LiFeAs: Density functional calculations, Phys. Rev. B **78**, 094511 (2008).

[56] J. Fink, S. Thirupathaiah, R. Ovsyannikov, H. A. Dürr, R. Follath, Y. Huang, S. de Jong, M. S. Golden, Y.-Z. Zhang, H. O. Jeschke, R. Valentí, C. Felser, S. Dastjani Farahani, M. Rotter, and D. Johrendt, Electronic structure studies of $BaFe_2As_2$ by angle-resolved photoemission spectroscopy, Phys. Rev. B **79**, 155118 (2009).

[57] D. Wu, N. Barišić, P. Kallina, A. Faridian, B. Gorshunov, N. Drichko, L. J. Li, X. Lin, G. H. Cao, Z. A. Xu, N. L. Wang, and M. Dressel, Optical investigations of the normal and superconducting states reveal two electronic subsystems in iron pnictides, Phys. Rev. B **81**, 100512(R) (2010).

[58] Z. P. Yin, K. Haule, and G. Kotliar, Magnetism and charge dynamics in iron pnictides, Nat. Phys. **7**, 294 (2011).

[59] R. A. Ferrell and R. E. Glover, Conductivity of Superconducting Films: A Sum Rule, Phys. Rev. **109**, 1398 (1958).

[60] M. Tinkham and R. A. Ferrell, Determination of the Superconducting Skin Depth from the Energy Gap and Sum Rule, Phys. Rev. Lett. **2**, 331 (1959).

[61] C. C. Homes, Y. M. Dai, J. S. Wen, Z. J. Xu, and G. D. Gu, $FeTe_{0.55}Se_{0.45}$: A multiband superconductor in the clean and dirty limit, Phys. Rev. B **91**, 144503 (2015).

[62] C. C. Homes, S. V. Dordevic, M. Strongin, D. A. Bonn, R. Liang, W. N. Hardy, S. Komiya, Y. Ando, G. Yu, N. Kaneko, X. Zhao, M. Greven, D. N. Basov, and T. Timusk, Universal scaling relation in high-temperature superconductors, Nature (London) **430**, 539 (2004).

[63] C. C. Homes, S. V. Dordevic, D. A. Bonn, R. Liang, W. N. Hardy, and T. Timusk, Coherence, incoherence, and scaling along the c axis of $YBa_2Cu_3O_{6+x}$, Phys. Rev. B **71**, 184515 (2005).

[64] C. C. Homes, S. V. Dordevic, T. Valla, and M. Strongin, Scaling of the superfluid density in high-temperature superconductors, Phys. Rev. B **72**, 134517 (2005).

[65] J. J. Tu, J. Li, W. Liu, A. Punnoose, Y. Gong, Y. H. Ren, L. J. Li, G. H. Cao, Z. A. Xu, and C. C. Homes, Optical properties of the iron arsenic superconductor $BaFe_{1.85}Co_{0.15}As_2$, Phys. Rev. B **82**, 174509 (2010).

[66] R. Yang, Y. Dai, J. Yu, Q. Sui, Y. Cai, Z. Ren, J. Hwang, H. Xiao, X. Zhou, X. Qiu, and C. C. Homes, Unravelling the mechanism of the semiconducting-like behavior and its relation to superconductivity in $(CaFe_{1-x}Pt_xAs)_{10}Pt_3As_8$, Phys. Rev. B **99**, 144520 (2019).

[67] N. V. Smith, Classical generalization of the Drude formula for the optical conductivity, Phys. Rev. B **64**, 155106 (2001).

[68] Replacing the broad Drude term with the expression in Eq. (2) and fitting to the real and imaginary parts of the optical conductivity using a nonlinear least-squares technique yields $\omega_p \simeq 5350\ \mathrm{cm}^{-1}$, $1/\tau \simeq 146\ \mathrm{cm}^{-1}$, and $c = -0.7$. The plasma frequency is larger because it now describes both the localized and free carriers; $\omega_p^2 \simeq \omega_{p,D2}^2 + \Omega_0^2$.

[69] Y. M. Dai, B. Xu, B. Shen, H. H. Wen, J. P. Hu, X. G. Qiu, and R. P. S. M. Lobo, Pseudogap in underdoped $Ba_{1-x}K_xFe_2As_2$ as seen via optical conductivity, Phys. Rev. B **86**, 100501(R) (2012).

[70] V. B. Zabolotnyy, D. S. Inosov, D. V. Evtushinsky, A. Koitzsch, A. A. Kordyuk, G. L. Sun, J. T. Park, D. Haug, V. Hinkov, A. V. Boris, C. T. Lin, M. Knupfer, A. N. Yaresko, B. Büchner, A. Varykhalov, R. Follath, and S. V. Borisenko, (π,π) electronic order in iron arsenide superconductors, Nature (London) **457**, 569 (2009).

[71] G. Derondeau, F. Bisti, M. Kobayashi, J. Braun, H. Ebert, V. A. Rogalev, M. Shi, T. Schmitt, J. Ma, H. Ding, V. N. Strocov, and J. Minár, Fermi surface and effective masses in photoemission response of the $(Ba_{1-x}K_x)Fe_2As_2$ superconductor, Sci. Rep. **7**, 8787 (2017).

[72] M. Yi, D. H. Lu, J. G. Analytis, J.-H. Chu, S.-K. Mo, R.-H. He, M. Hashimoto, R. G. Moore, I. I. Mazin, D. J. Singh,

Z. Hussain, I. R. Fisher, and Z.-X. Shen, Unconventional electronic reconstruction in undoped (Ba,Sr)Fe_2As_2 across the spin density wave transition, Phys. Rev. B **80**, 174510 (2009).

[73] F. Wooten, *Optical Properties of Solids* (Academic, New York, 1972), pp. 244–250.

[74] M. Dressel and G. Grüner, *Electrodynamics of Solids* (Cambridge University Press, Cambridge, 2001).

[75] D. J. Singh, *Planewaves, Pseudopotentials and the LAPW method* (Kluwer Adademic, Boston, 1994).

[76] D. Singh, Ground-state properties of lanthanum: Treatment of extended-core states, Phys. Rev. B **43**, 6388 (1991).

[77] P. Blaha, K. Schwarz, G. K. H. Madsen, D. Kvasnicka, and J. Luitz, *WIEN2k, an augmented plane wave plus local orbitals program for calculating crystal properties* (Technische Universität Wien, Austria, 2001).